Research Paper

Implementation of a Cost-Effective, Accurate Photoacoustic Imaging System Based on High-Power LED Illumination and FPGA-Based Circuitry

Maryam AHANGAR DARBAND, Esmaeil NAJAFIAGHDAM*

Department of Electrical Engineering, Sahand University of Technology
Tabriz, Iran

*Corresponding Author e-mail: najafiaghdam@sut.ac.ir

Imaging based on the photoacoustic (PA) phenomenon is a type of hybrid imaging approach that combines the advantages of pure optical and pure acoustic imaging, achieving good results. This method, which offers high resolution, suitable contrast, and non-ionizing radiation, is valuable for the early detection of various types of cancer. Recently, multiple studies have focused on improving different components of this imaging system. In this presentation, we implemented a simplest form of a PA imaging system for detecting blood vessels, given that angiogenesis is recognized as a common symptom of many cancers. For the first time, we implemented a high-power light-emitting diode (LED), to replace bulky and expensive lasers, and integrated circuit technologies such as field-programmable gate arrays (FPGAs) for a simple LED driver circuit and data acquisition (DAQ). Using an FPGA block, we successfully generated a 200-ns square pulse wave with a repetition frequency of 25 kHz, whose amplified form can drive a high-power LED at 1050 nm for appropriately stimulating the sample. By using ultrasonic sensors with a central frequency of 1 MHz and a DAQ system with 16-bit accuracy, along with a suitable algorithm for image reconstruction, we successfully detected blood vessels in a breast tissue mimic. With the use of the FPGA-based block, the image reconstruction algorithm was accelerated. Finally, the simultaneous and first-time use of LED and FPGA-based circuit technology for driving the LED, output information processing and image reconstruction were performed in PA imaging.

Keywords: photoacoustic imaging (PAI); light emitting diode (LED); pulsed light; breast tumor; field-programmable gate array (FPGA).

1. Introduction

A wide variety of imaging methods are involved in the diagnostic process. They include X-rays, computed tomography (CT), and magnetic resonance imaging (MRI), which can help to pinpoint diagnoses and rule out other conditions that may be causing symptoms. However, our primary focus is on non-invasive, accessible, inexpensive, and highly accurate imaging modalities. Hybrid imaging methods that combine the advantages of multiple methods seem to be promising options. One such hybrid imaging modality is photoacoustic imaging (PAI), which detects optical absorption contrast acoustically via the PA effect (XU, WANG, 2006). In PAI, nanosecond and non-ionizing pulsed lasers with relatively high energy [mJ] are directed at the sample. Then, a portion of this energy is absorbed and converted into heat, leading to thermoelastic expansion and, consequently, the propagation of wideband ultrasonic waves [MHz] (WANG, 2008).

The physics of the PA phenomenon has been thoroughly studied in our previous works (AHANGAR DARBAND *et al.*, 2023a; 2023b); here, we provide a brief overview. The general equation describing the PA phenomena can be expressed as follows:

$$\left[\nabla^2 - \frac{1}{v_s^2}\frac{\partial^2}{\partial t^2}\right]p(rt) = -\frac{p_0}{v_s^2}\frac{\partial \delta(t)}{\partial t}, \qquad (1)$$

where the acoustic wave is the $p(r,t)$ at position (r) and time (t), initiated by an initial source $p_0(r) = \Gamma(r)A_e(r)$, where $A_e(r)$ is the spatial electromagnetic (EM) absorption function, v_s is the speed of sound, and

$\Gamma(r) = v_s^2\beta/C_p$ is the Grüneisen parameter, defined by the following parameters: $\beta = (1/V)(\partial V/\partial T)_p$, where V is the volume, T is the temperature, p is the ambient density, and C_p is the specific heat. To improve the optimal feature of the PA signal, several factors must be considered: stimulation with pulsed radiation at nanosecond [ns] duration, stress confinement, and thermal confinement (AHANGAR DARBAND *et al.,* 2023a; 2023b). During the past decade, extensive efforts have been made to improve the performance of various components of PAI (PALTAUF *et al.,* 2020). PAI has a range of applications in medicine, including tissue imaging, functional imaging, and molecular imaging (PONIKWICKI *et al.,* 2019; LINDE *et al.,* 2014). However, our focus in this report is on breast tissue imaging using the PA phenomenon for breast tumor diagnosis, as breast cancer is one of the most common cancers (American Cancer Society, 2019) and if it can be detected early in time, its treatment will be easier. Therefore, we intend to use the PAI system for the early detection of breast tumors.

The PAI system consists of four main components: 1) a stimulation light generation block and a channel for conversion of emitted light into a uniform, homogenized output (HARDER *et al.,* 2004); 2) a sample, which can be either real tissue or a tissue mimic; 3) ultrasonic sensors collecting the propagated ultrasonic wave; 4) a DAQ card combined with an image reconstruction algorithm to convert the captured data into images.

Despite the progress and improvements made in various aspects of PAI over recent decades, there remains room for further improvements in several components of this method. We have previously published the simulation results for different parts of the PAI system on different platforms (AHANGAR DARBAND *et al.,* 2023a), as well as studies on our proposed image reconstruction algorithm in separate research works (AHANGAR DARBAND *et al.,* 2023b). However, this review aims to show our practical implementation of a breast tissue PAI system that is designed to be as simple and cost-effective as possible (FATIMA *et al.,* 2019). One of the most important components of the PAI system is the sample stimulation module (TAM, 1986). Some optical sources commonly used as excitation modules in PAI include lasers, such as the Q-switched Nd:YAG laser (KHOSROSHAHI, MANDELIS, 2015), diode laser, optical parametric oscillator laser system, frequency-doubled YAG laser, and Ti:sapphire laser (WANG, 2017). However, there are some disadvantages to the laser stimulation system. They include high price, bulky size, complexity in both laser device structure and driving circuit, and a requirement to use a dedicated wrapped light homogenization system (XAVIERSELVAN, MALLIDI, 2020). It has previously been reported that high-power LED can serve as an alternative excitation source for PAI (HANSEN, 2011;

ZHU *et al.,* 2020; ALLEN, BEARD, 2016) given their low-cost (tens of dollars), ease of integration, and smaller size. Therefore, to leverage these advantages of high-power LED, we used a high-power LED in our PAI stimulation module. Based on the findings in (AGRAWAL *et al.,* 2021), although LEDs provide lower output energy than laser, their high pulse repetition rate offers the possibility to average more frames and thus improve the signal-to-noise ratio (SNR). LED-based PAI holds strong potential for point-of-care PA imaging, where an imaging depth of 2 cm–3 cm is sufficient (JO *et al.,* 2020). In addition to the benefits of using LED, the circuit presented in this article for LED driving is as simple as possible due to the use of a field programmable gate array (FPGA)-based module, further reducing system complexity.

The use of real tissue in studies of the implemented system would significantly help in the detailed analysis of the captured data. But, due to possible unwanted concerns, in this report, we used a tissue-mimic sample to test the device.

The induced PA signal was detected by ultrasonic transducers and then amplified and acquired by a DAQ card to modify signals for use in the MATLAB environment, where they were processed using an image reconstruction algorithm. Actually, the LED driving circuits, digital signal processing, recording, and reconstruction were all implemented using an FPGA-based hardware system. This approach allowed us to establish a PAI system in the simplest possible form (UPPUTURI, PRAMANIK, 2017; LIU *et al.,* 2023).

The image reconstruction algorithm is the most important component of a PAI system, as it determines sensitivity, speed, and resolution (WANG, 2017). In our previous work (AHANGAR DARBAND *et al.,* 2023ab), we reviewed different image reconstruction algorithms and presented our own algorithm. Since this article mainly focuses on the practical setup of the imaging system based on the PA phenomenon, we do not go into the details of the image reconstruction algorithm. Tailored to the geometry of the imaging system, the algorithm used in this study was based on a phase-controlled algorithm (ZHOU *et al.,* 2011).

2. Principles and construction

2.1. Proposed method

We describe a simple and cost-effective PAI system that can be used for in vitro mapping of breast tissue mimics. For a detailed description of the different components of the proposed PAI system see Fig. 1.

To propagate detectable PA waves, the light irradiated to the tissue should be short-pulsed or modulated with specific energy levels. Also, a proper wavelength must be selected to detect specific markers in breast tissue and tumor (WANG, 2017). Among the commer-
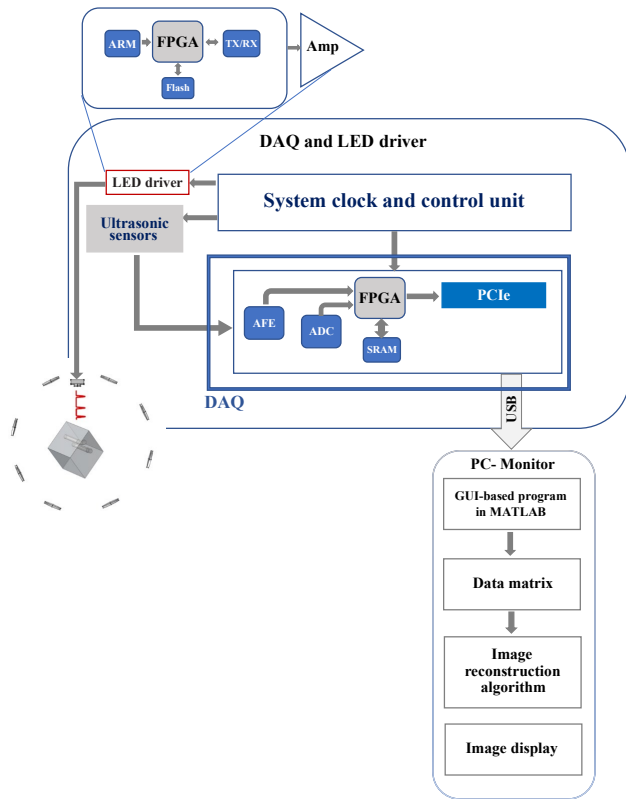
Fig. 1. Block diagram of the proposed implemented system.

cially available LEDs, we used an infrared high-power LED (LZ1-10R802, OSRAM). Easy-to-use evaluation circuit and cooling system enabled by FPGA-based technology, a low price (only a few tens of dollars), and small dimensions are the most important advantages of these LEDs. The LED driver circuit consists of an FPGA module and a wide-band two-stage amplifier. The FPGA-based LED driver circuit used in this work offers greater flexibility and speed capabilities compared to traditional MOSFET-based LED driver circuits (Zhu *et al.*, 2020; Liu *et al.*, 2023).

With the help of an FPGA-based module (Mojo Plus – FPGA Spartan 6) and appropriate programming of the FPGA, the required pulsed signal could be generated from the Mojo output pins. In our LED driving circuit, the Mojo module was programmed to generate a 200 ns square pulse (proper pulse to satisfy the stress confinement criteria (Wang, 2008). This pulse features a rise-time of 1.9 ns, a fall-time of 3.7 ns, and a repetition rate of 25 kHz (Fig. 2). Afterward, the voltage amplitude of the pulse was amplified to the necessary level for optimal LED operation. Our two-stage wideband amplifier (designed and manufactured by the Microelectronics Laboratory of Sahand University) provides a wide dynamic range with high output voltage and high current. This amplifier was designed using a very high-speed, high-output current, high-voltage feedback amplifier integrated circuit (IC) (LM7171).
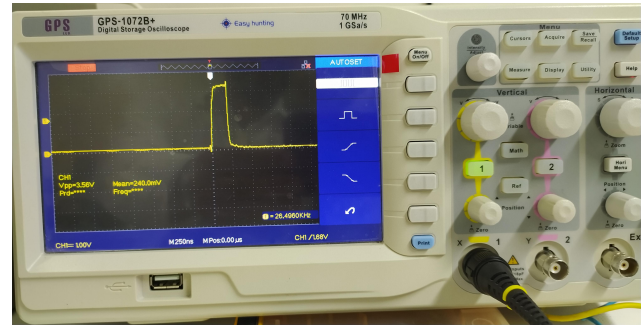

Fig. 2. LED driving pulse wave: a 200 ns square pulse with a repetition rate of 25 kHz.

It offers an adjustable gain between 22 and 150, with a maximum operating frequency of 12 MHz for the digital input. Additionally, the maximum output current is 120 mA. Finally, the driven LED radiates to an area of 1 mm $\times$1 mm with a power output of 1.2 W at a wavelength of 1050 nm, which is the appropriate absorption wavelength for PAI (Wang, 2017). Since the LED is placed in the water environment of the test chamber, its internal circuit, ensuring no obstruction to its radiation, is completely sealed within plastic containers. For complete tomography, the LED can rotate 270° around the sample at a distance of 5 mm from the tissue and can move along a straight line approximately 2 cm in length along the z-axis. A schematic representation in Fig. 3 illustrates the structure and geometry of this radiation block.
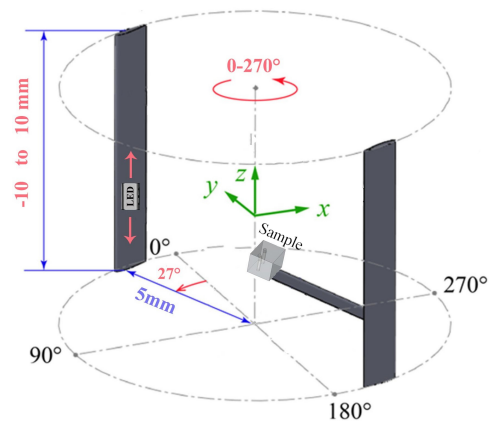

Fig. 3. Schematic structure and geometry of the radiation block.

Breast cancer is often associated with angiogenesis, and diagnosing abnormal blood vessels in the tissue seems to be the best shortcut for diagnosing breast tumors (American Cancer Society, 2019). Accordingly, a mimic breast tissue model with blood vessels was created in such a way that two low-density polyethylene (LDPE) tubes with an inner diameter of 1 mm were embedded in the middle and along the side edge of a chicken breast tissue (a square cube approximately 2 cm long) at a depth of 3 mm. These tubes were filled

with human blood that had been treated with heparin (0.1 mg/ml–0.2 mg/ml low-molecular-weight heparin (LMWH)) as an anticoagulant (Fig. 4). To determine imaging accuracy, a portion of the tube was emptied. Also, to accurately study the PAI system, we focused solely on the mimic blood vessel. The sample was fixed 5 mm in front of the LED radiation in an aqueous environment to optimize ultrasonic coupling between the sample and the ultrasonic transducer.

Fig. 5. Schematic of ultrasonic sensors with a central frequency of 1 MHz and a focal length of 66.74 mm.

signal around the circular area of the cross-section of the cylindrical chamber. The cylindrical chamber has a diameter of 8 cm and a height of 14 cm, with the sensors placed 6 cm above the bottom of the chamber (see Figs. 6–7).

a)

b)

Fig. 6. Top view of the test sample chamber and the arrangement of the eighth sensors, sample, and LED simulated in COMSOL.
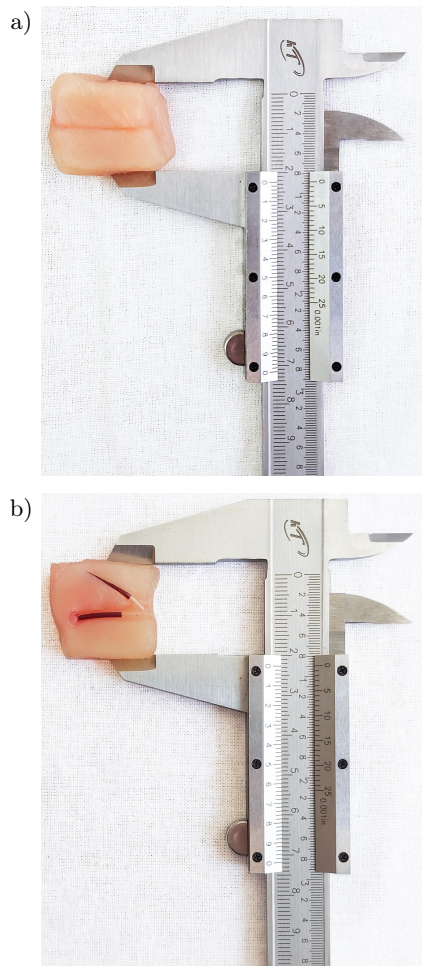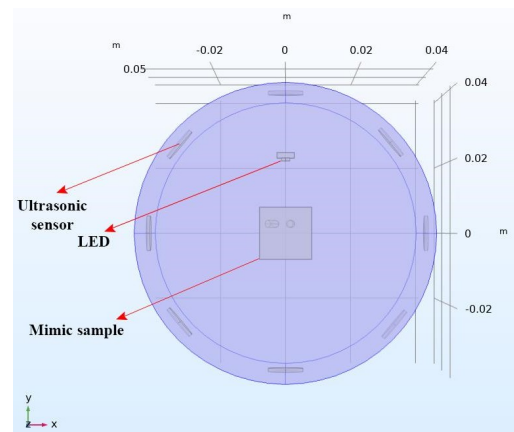

Fig. 4. Breast tissue-mimicking phantoms: a) chicken breast model with dimensions of 2 cm × 2 cm diameter; b) LDPE tubes embedded as vessels filled with blood inoculated with heparin as an anticoagulant.

The signals received by the ultrasonic sensors contain important information about the properties of the tissue being imaged. The process of receiving, processing, and transmitting the appropriate data to MATLAB to reconstruct the images was done by an analog front-end block. The PA signal propagated from the tissue were detected by eight ultrasonic sensors (PSC1.0M014083H2AD2-B0, Zhejiang Jiakang Electronics Co., Ltd.) with a central frequency of 1 MHz (1.0 MHz ±0.1 MHz) and a focal length of 66.74 mm (Fig. 5). These eight ultrasonic sensors were arranged at equal distances from each other to receive the PA
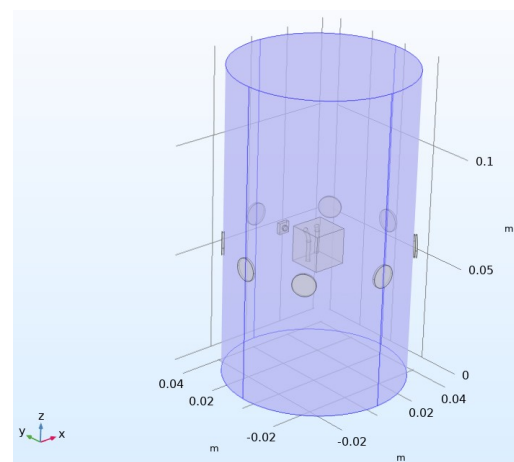
Fig. 7. Side view of the layout of the test chamber simulated in COMSOL. The mimic blood vessels inside the sample are visible in this view.
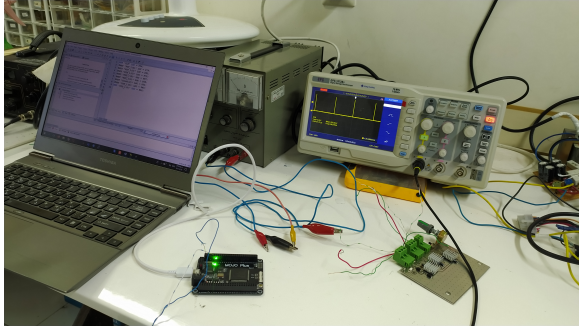
Fig. 8. View of the implemented system in the laboratory.

A DAQ (PC7KS02, Rizpardaz Electronics Company) was used to properly process the data on which Xilinx Spartan™ 7 FPGA was located. It comprises eight input channels to receive analog PA signals, which are connected to the rest of the circuit with four analog-to-digital (ADC) converters. The sampling frequency of these ADC is up to 250 million samples per second and has an accuracy of 14 bits to 16 bits. In our proposed PAI system, the sampling rate is equal to 50 million samples per second, which provides 16-bit data at the output of the ADC. The digital signal is saved inside the FPGA and then transmitted to the computer at a speed of 1 million bit/s through the network interface. In the MATLAB environment, a graphical user interface (GUI) has been developed to easily view and draw the received data. The LED driver circuit and GUI saving data in proper time are in complete synchronization.

Choosing the right algorithm based on the scanning geometry is a critical task that significantly affects image reconstruction accuracy and speed. Based on the structure of the presented here system, we used a spatial phase-controlled algorithm (ZHOU *et al.*, 2011) to reconstruct the images. We also used the FPGA-based platform to accelerate the image reconstruction speed (GAO *et al.*, 2022). To obtain enough information about the tissue structure and accurately detect blood vessels, stimulation was done from various directions. The light source was moved at different angles and along the *z*-axis. At first, the LED was placed 5 mm from the sample and its opposite point, and then it was rotated by ten 27° counterclockwise rotations from its initial position. This 270° rotation is repeated five times around the sample in a straight line, along the *z*-axis at 4 mm intervals ranging from −10 mm to 10 mm.

After processing and sampling, the data captured from the ultrasonic sensors were entered into MATLAB as 50 matrices with dimensions of 8 × 1019. The feasibility of our PAI system was first validated by diagnosing vessels in tissue-mimicking phantoms. The following section presents the results of tissue tomography in the form of two-dimensional slices, which were the output of the image reconstruction algorithm.

3. Results

To demonstrate the potential of our proposed PAI system and its accuracy in detecting vessels in the mimic tissue, two scenarios were tested: 1) two vessels and 2) a single vessel embedded in the mimic tissue. In the first case, where two vessels were included in the mimic tissue, we used the sample shown in Fig. 4b. As previously described, 50 different positions were considered for LED placement. Figure 9 displays the results of image reconstruction by processing the information captured by the sensors in these modes. The total computation time for each image was 1 minute and 55.52 seconds. Figures 10 and 11 depict the output data from the sensors for the first scenario, where two mimic vessels were embedded in the sample, and the LED was positioned at point $Z = 0$, directly in front of the sample. Figure 10 shows the sensor data as an image using the full range of colormap colors to illustrate data intensity over time at each sensor position. Figure 11 presents each sensor's normalized data plotted against time for the same LED position. The procedure was then repeated for the second scenario in which only one mimic vessel was placed inside the sample (Fig. 12). The processed sensor data for the single
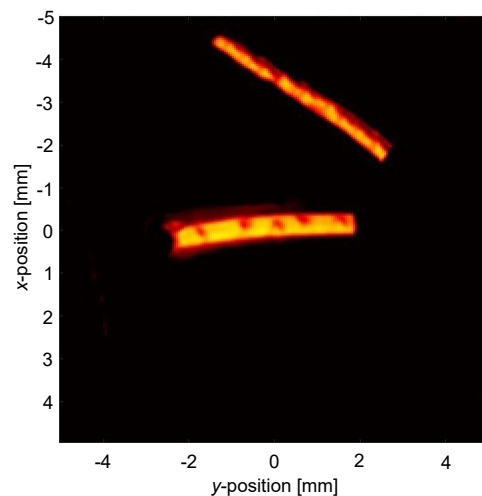

Fig. 9. Output from the image reconstruction algorithm for the case in which two mimic vessels were embedded in the sample.
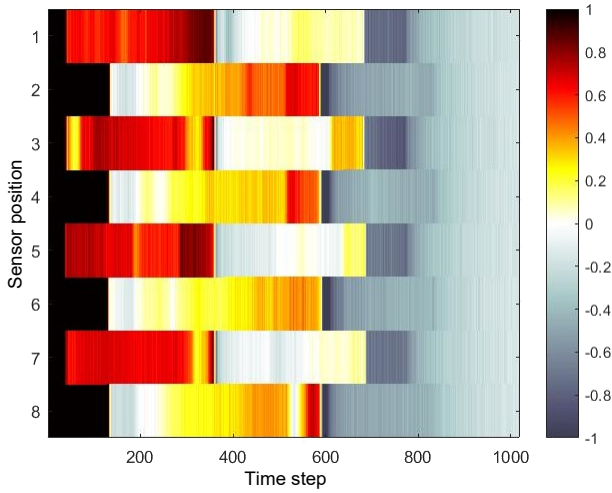
Fig. 10. Display of the sensor data as an image using the full range of colors in the colormap in the first case.
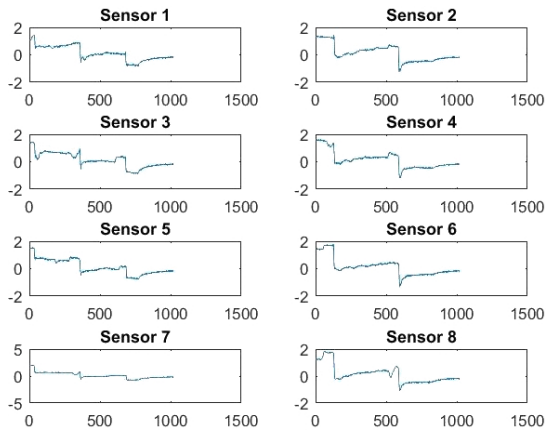

Fig. 11. Plotting of each sensor's normalized data graph against time [s] separately in the first state.
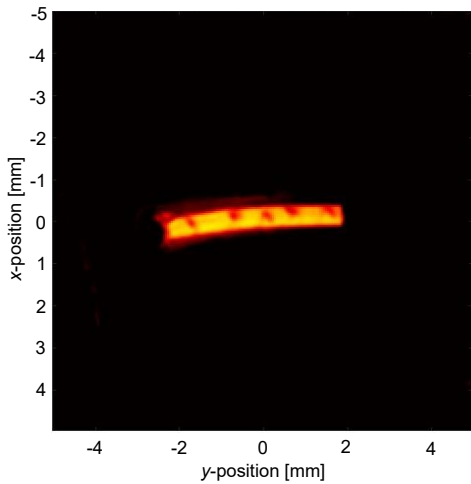

Fig. 12. Output of the image reconstruction algorithm output for the case in which one mimic vessel was embedded in the sample.

mimic vessel case is shown in Fig. 13, utilizing the full colormap range for clarity. In addition, the normalized data for each individual sensor in the second case is
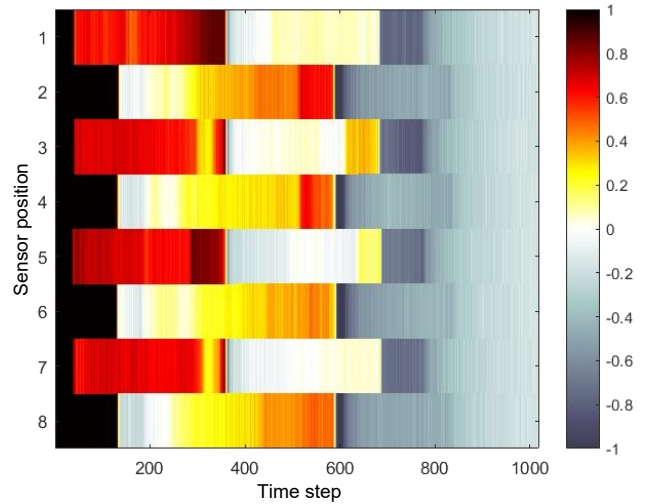

Fig. 13. Display of the sensor data as an image using the full range of colors in the colormap in the second case, testing a mimic vessel embedded in the sample.

shown in Fig. 14. This figure presents the sensor outputs over time, highlighting how the signal patterns differ with a single mimic vessel in the sample, compared to the two-vessel configuration in the first scenario (Fig. 11).
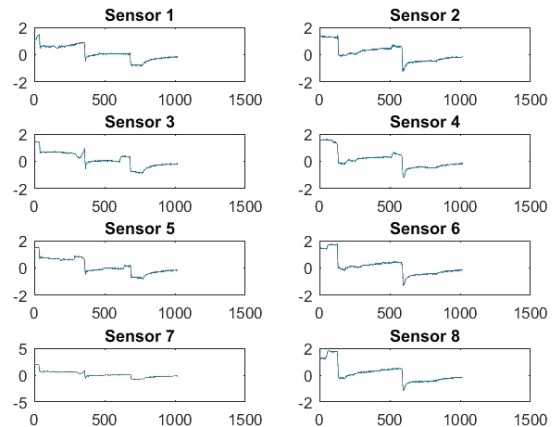

Fig. 14. Plotting of each sensor's normalized data graph against time [s] separately in the second case.

Based on the results presented, this report utilized a high-power LED to achieve good penetration depth. We generated a suitable pulse todrive the LED using FPGA technology, which successfully met the stress confinement requirements and generated efficient acoustic waves.

4. Conclusion

In summary, this article demonstrated the implementation of a miniature PAI system capable of detecting blood vessels at a depth of 3 mm using using high-power LED radiation, a driving circuit, and data

acquisition (DAQ) based on FPGA technology. The simple, low-cost, and compact setup makes it possible to conveniently use it in non-invasive and label-free diagnoses. Furthermore, in future work, by using high-power LEDs in arrays (Van Heumen *et al.*, 2023; Joseph *et al.*, 2020) or specialized light delivery system (Kuriakose *et al.*, 2020), we could enhance the accuracy and depth of the system's diagnostic capabilities and overcome many problems associated with using LEDs (Zhu *et al.*, 2020) in PAI systems.

Supplemental material

The data that support the findings of this study are available from the corresponding author upon reasonable request.

References

1. Agrawal S., Kuniyil Ajith Singh M., Johnstonbaugh K., Han D.C., Pameijer C.R., Kothapalli S.-R. (2021), Photoacoustic imaging of human vasculature using LED versus laser illumination: A comparison study on tissue phantoms and in vivo humans, *Sensors*, **21**(2): 424, https://doi.org/10.3390/s21020424.

2. Ahangar Darband M., Najafi Aghdam E., Gharibi A. (2023a), Numerical simulation of breast cancer in the early diagnosis with actual dimension and characteristics using photoacoustic tomography, *Archives of Acoustics*, **48**(1): 25–38, https://doi.org/10.24425/aoa.2023.144263.

3. Ahangar Darband M., Qorbani O., Najafi Aghdam E. (2023b), Modified algebraic reconstruction technique based on circular scanning geometry to improve processing time in photoacoustic tomography, *Microwave and Optical Technology Letters*, **65**(8): 2456–2463, https://doi.org/10.1002/mop.33714.

4. Allen T.J., Beard P.C. (2016), High power visible light emitting diodes as pulsed excitation sources for biomedical photoacoustics, *Biomedical Optics Express*, **7**(4): 1260–1270, https://doi.org/10.1364/BOE.7.001260.

5. American Cancer Society (2019), *Breast cancer facts & figures 2019–2020*, Atlanta: Cancer Society, Inc.

6. Fatima A. *et al.* (2019), Review of cost reduction methods in photoacoustic computed tomography, *Photoacoustics*, **15**: 100137, https://doi.org/10.1016/j.pacs.2019.100137.

7. Gao Z., Shen Y., Jiang D., Liu F., Gao F., Gao F. (2022), FPGA acceleration of image reconstruction for real-time photoacoustic tomography, ArXiv preprint, https://doi.org/10.48550/arXiv.2204.14084.

8. Hansen R.S. (2011), Using high-power light emitting diodes for photoacoustic imaging, [in:] *Medical Imaging 2011: Ultrasonic Imaging, Tomography, and Therapy*, **7968**: 83–88, https://doi.org/10.1117/12.876516.

9. Harder I., Lano M., Lindlein N., Schwider J. (2004), Homogenization and beam shaping with microlens arrays, [in:] *Photon Management*, **5456**: 99–107, https://doi.org/10.1117/12.549015.

10. Jo J., Xu G., Schiopu E., Chamberland D., Gandikota G., Wang X. (2020), Imaging of enthesitis by an LED-based photoacoustic system, *Journal of Biomedical Optics*, **25**(12): 126005, https://doi.org/10.1117/1.JBO.25.12.126005.

11. Joseph Francis K., Boink Y.E., Dantuma M., Ajith Singh M.K., Manohar S., Steenbergen W. (2020), Tomographic imaging with an ultrasound and LED-based photoacoustic system, *Biomedical Optics Express*, **11**(4): 2152–2165, https://doi.org/10.1364/BOE.384548.

12. Khosroshahi M.E., Mandelis A. (2015), Combined photoacoustic ultrasound and beam deflection signal monitoring of gold nanoparticle agglomerate concentrations in tissue phantoms using a pulsed Nd:YAG laser, *International Journal of Thermophysics*, **36**: 880–890, doi: https://doi.org/10.1007/s10765-014-1773-3.

13. Kuriakose M., Nguyen C.D., Kuniyil Ajith Singh M., Mallidi S. (2020), Optimizing irradiation geometry in LED-based photoacoustic imaging with 3D printed flexible and modular light delivery system, *Sensors*, **20**(13): 3789, https://doi.org/10.3390/s20133789.

14. Linde B.B.J., Sikorska A., Śliwiński A., Żwirbla W. (2014), Molecular association and relaxation phenomena in water solutions of organic liquids examined by photoacoustic and ultrasonic methods, *Archives of Acoustics*, **31**(4(S)): 143–152.

15. Liu X., Kalva S.K., Lafci B., Nozdriukhin D., Deán-Ben X.L., Razansky D. (2023), Full-view LED-based optoacoustic tomography, *Photoacoustics*, **31**: 100521, https://doi.org/10.1016/j.pacs.2023.100521.

16. Paltauf G., Nuster R., Frenz M. (2020), Progress in biomedical photoacoustic imaging instrumentation toward clinical application, *Journal of Applied Physics*, **128**(18): 180907, https://doi.org/10.1063/5.0028190.

17. Ponikwicki N. *et al.* (2019), Photoacoustic method as a tool for analysis of concentration-dependent thermal effusivity in a mixture of methyl alcohol and water, *Archives of Acoustics*, **44**(1): 153–160, https://doi.org/10.24425/aoa.2019.126361.

18. Van Heumen S., Riksen J.J., Singh M.K.A., Van Soest G., Vasilic D. (2023), LED-based photoacoustic imaging for preoperative visualization of lymphatic vessels in patients with secondary limb lymphedema, *Photoacoustics*, **29**: 100446, https://doi.org/10.1016/j.pacs.2022.100446.

19. Tam A.C. (1986), Applications of photoacoustic sensing techniques, *Reviews of Modern Physics*, **58**(2): 381, https://doi.org/10.1103/RevModPhys.58.381.

20. Upputuri, P.K., Pramanik M. (2017), Recent advances toward preclinical and clinical translation of photoacoustic tomography: A review, *Journal of Biomedical Optics*, **22**(4): 041006, https://doi.org/10.1117/1.JBO.22.4.041006.

21. Wang L.V. [Ed.] (2017), *Photoacoustic Imaging and Spectroscopy*, CRC Press.

22. Wang L.V. (2008), Prospects of photoacoustic tomography, *Medical Physics*, **35**(12): 5758–5767, https://doi.org/10.1118/1.3013698.

23. Xavierselvan M., Mallidi S. (2020), LED-based functional photoacoustics – Portable and affordable solution for preclinical cancer imaging [in:] *LED-Based Photoacoustic Imaging: From Bench to Bedside*, pp. 303–319, https://doi.org/10.1007/978-981-15-3984-8_12.

24. Xu M., Wang L.V. (2006), Photoacoustic imaging in biomedicine, *Review of Scientific Instruments*, **77**(4): 041101, https://doi.org/10.1063/1.2195024.

25. Zhu Y. *et al.* (2020), Towards clinical translation of LED-based photoacoustic imaging: A review, *Sensors*, **20**(9): 2484, https://doi.org/10.3390/s20092484.

26. Zhou Q., Ji X., Xing D. (2011), Full-field 3D photoacoustic imaging based on plane transducer array and spatial phase-controlled algorithm, *Medical Physics*, **38**(3): 1561–1566, https://doi.org/10.1118/1.3555036.